UC Davis
UC Davis Previously Published Works

Title

Assessing the Impact of Spatial Resolution on the Estimation of Leaf Nitrogen Concentration Over the Full Season of Paddy Rice Using Near-Surface Imaging Spectroscopy Data

Permalink

https://escholarship.org/uc/item/6gp6b9kg

Authors

Zhou, Kai
Cheng, Tao
Zhu, Yan
et al.

Publication Date

2018

DOI

10.3389/fpls.2018.00964

Peer reviewed

eScholarship.org Powered by the California Digital Library
University of California

Assessing the estimation of leaf nitrogen concentration over the full season of paddy rice using multi-scale imaging spectroscopy data

Kai Zhou[a,b], *Tao Cheng*[a,], *Yan Zhu*[a], *Weixing Cao*[a,*], *Hengbiao Zheng*, *Xia Yao*[a], *Yongchao Tian*[a], *Susan L. Ustin*[b]

[a] National Engineering and Technology Center for Information Agriculture, Key Laboratory for Crop System Analysis and Decision Making, Ministry of Agriculture, Jiangsu Key Laboratory for Information Agriculture, Jiangsu Collaborative Innovation Center for Modern Crop Production, Nanjing Agricultural University, Nanjing 210095, China

[b] Center for Spatial Technologies and Remote Sensing (CSTARS), Department of Land, Air, and Water Resources, University of California, Davis, CA 95616-8617, USA

* To whom correspondence should be addressed. E-mail addresses: caow@njau.edu.cn (W. Cao, Tel: +86-25-8439-6598); fax: +86-25-8439-6672.

July 15, 2017

Abstract

Keywords:

1. Introduction

2. Materials and Methods

2.1. Experimental design

Two rice (*Oryza sativa* L.) experiments were designed, encompassing a combination of treatments in rice cultivar, planting density and N rate. These two experiments were respectively conducted in 2014 and 2015 from July to September at the experimental station of National Engineering and Technology Center for Information Agriculture (NETCIA), Rugao, Jiangsu, China (120°19′ E, 32°14′ N) with same treatments for each year. The predominant soil texture was loam and the organic carbon concentration in soil was 12.95 $g \cdot kg^{-1}$. The annual average temperature was 14.6 °C and annual average precipitation was 1055.5 mm, respectively.

Four N fertilization rates [0 (N0), 100 (N1), 200 (N2) and 300 (N3) kg N ha^{-1}] were applied in the form of urea, with 40% at preplanting, 10% at tillering, 30% at jointing and 20% at booting. In particular, there were two planting densities (0.30 m by 0.15 m and 0.50 m by 0.15 m) for N1 and N2 rates and one planting density (0.30 m by 0.15 m) for N0 and N3 rates. Each treatment had three replicates which were arranged in a randomized block design. For all plots, 135 kg P_2O_5 ha^{-1} (as phosphate fertilizer) and 190 kg K_2O ha^{-1} (as potassium fertilizer) were applied before transplanting. The two rice cultivars were Japonica rice with erect plant type, Wuyunjing 24 (V1) and Indica rice with spread type, Y liangyou 1 (V2). Each plot size was 5 m

by 6 m and a total of 36 plots (12 cultivation conditions with three replications) were grown in each experiment.

2.2. Acquisition and preprocessing of hyperspectral imagery

2.2.1. Hyperspectral image data acquisition

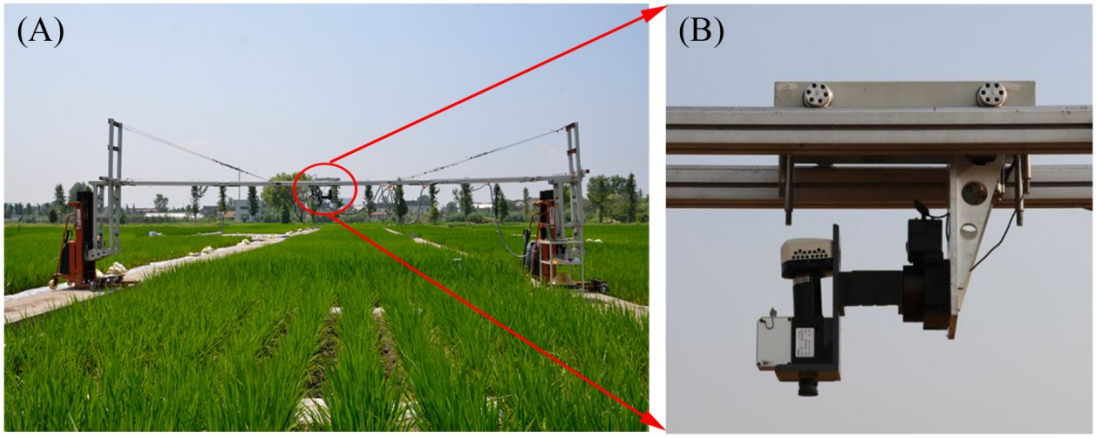

Fig. 1. (A) Experimental setup of the near-ground hyperspectral imaging system in the paddy field and (B) onset of the hyperspectral camera in the system.

Table 2

Summary of image acquisition dates (also denoted as days after transplanting: DAT) for the rice experiment.

Year	Early tillering	Late tillering	Jointing	Early booting	Late booting	Heading	Early filling	Late filling
2014	8 Jul. (22)	20 Jul. (34)	4 Aug. (49)	/	20 Aug. (65)	3 Sept. (78)	/	20 Sept. (96)
2015	9 Jul. (24)	21 Jul. (36)	31 Jul. (46)	14 Aug. (60)	25 Aug. (71)	/	9 Sept. (86)	/

All hyperspectral images were acquired by a pushbroom scanning sensor (ImSpector V10E-PS, SpecIm, Finland) mounted on a platform about 1.2 m above the rice canopies (**Fig. 1**). Our platform could be lifted up to a maximum height of 3 m above the ground and we could en-

sure fields of view in the same size at the top of canopy during the whole growing season. The spectral range of this sensor was from 360 nm to 1025 nm divided into 520 bands with a spectral resolution of 2.8 nm. The spatial dimension of image data was acquired by the movement of a linear actuator. The spatial resolution at near-nadir position (42.8° field of view) was about 1.3 mm and the swath width was about 0.9 m. The exposure time of this sensor was fixed manually to adapt to brightness variation between scans under natural light conditions, with approximately 40.2 ms for sunny days. This hyperspectral imaging system completed a scene by scanning rice canopies across the row orientation (5 m wide) and generated a total of 432 images for the two experiments. In particular, 36 images were collected for each growth stage (**Fig. 2**). The summary of image acquisition dates is shown in **Table 2.**

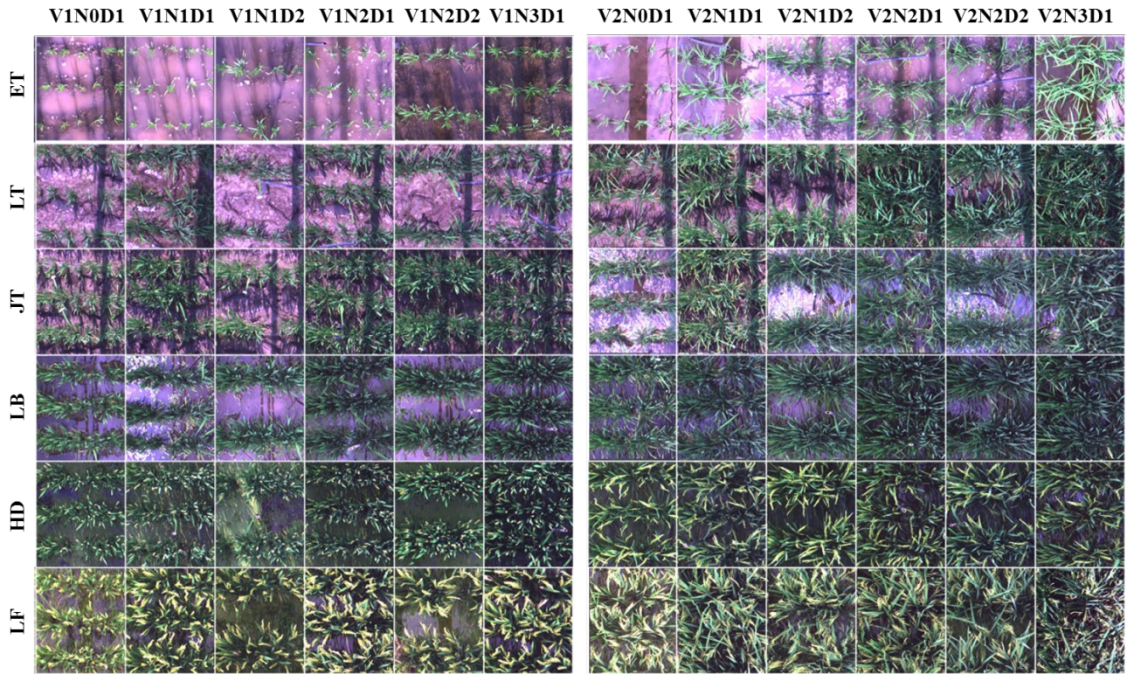

Fig. 2. Example true color images cropped from hyperspectral scenes acquired throughout the growing season in 2014. A total of 12 plots (one replication) for each growth stage were shown here. V1: Wuyunjing 24 (Japonica rice); V2: Y liangyou 1 (Indica rice). N0-N3: four N fertilization rates (0, 100, 200 and 300 kg·N·ha^{-1}). D1-D2: two row spacings (30 cm and 50 cm). ET: early tillering stage; LT: late tillering stage; JT: jointing stage; LB: late booting stage; HD: heading stage; LF: late filling stage.

2.2.2. Data preprocessing

The image preprocessing procedures including subtraction of sensor electronic noise (dark current) and radiometric correction were implemented within the specVIEW software (Specim, Oulu, Finland). The final relative reflectance values were converted from the original digital number (DN) values using the calibration equation as follows (Zhou et al., 2017):

$$Ref_{\text{target}} = \frac{DN_{\text{target}} - DN_{\text{noise}}}{DN_{\text{panel}} - DN_{\text{noise}}} \times Ref_{\text{panel}} \quad Ref_{target} = \frac{DN_{target} - DN_{noise}}{DN_{panel} - DN_{noise}} \quad Ref_{panel} \tag{1}$$

where DN_{target}, DN_{noise} and DN_{panel} is the DN value of target, electronic noise (dark current) and 99% reflective white reference panel, respectively. Ref_{target} and Ref_{panel} is the reflectance value of target and reference panel, respectively. A barium sulfate ($BaSO_4$) panel was placed on the tripod as the white reference panel. The relative reflectance data were smoothed using the Minimum Noise Fraction (MNF) transform procedure in the ENVI 4.8 (EXELIS, Boulder, CO, USA) software environment. The spectral data in the 400–900 nm range were retained because of strong noise in other spectral regions even after smoothing.

2.2.3. Image spatial subsampling

To avoid the BRDF effects on the left and right edges of images, we cropped original images and only used the middle half of the original images (i.e., the swath width was about 45 cm). The performance of LNC estimation was evaluated over various spatial resolutions. Given the swath width was 450 mm, we selected the spatial resolutions by dividing 450 mm by a factor of two iteratively. The original spatial resolutions of 1.3 mm was degraded to 2, 4, 7, 14, 28, 56, 113, 225 mm, 450 mm by aggregating over cells of N×N pixels as suggested in Jay et al. (2017). An example image at different spatial resolutions is illustrated in **Fig. 3**.

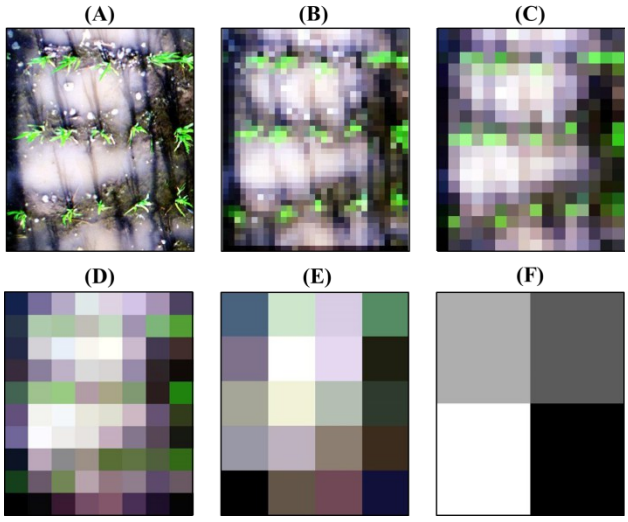

Fig. 3. Example true color images with gradual degradation of spatial resolution acquired on 8 July 2014. Illustration for (A) 1.3 mm, (B) 14 mm, (C) 28 mm, (D) 56 mm, (E) 113 mm and (F) 225 mm.

2.2.4. Discrimination of non-vegetation background and vegetation

To investigate the relationships between LNC and VIs derived from pure leaf pixels across the whole image at 1.3 mm spatial resolutions, we firstly identified vegetation pixels applying a threshold of the enhanced vegetation index (EVI) (Pinto et al., 2016; Zhou et al., 2017) (EVI > 0.45). Afterwards, we constructed the classification decision tree developed in Zhou et al. (2017) by applying photochemical reflectance index (PRI) (Gamon et al., 1992) and transformed chlorophyll absorption reflectance index (TCARI) (Haboudane et al., 2002) thresholds at two sequential steps for discriminating all the pixels of sunlit and shaded canopy organs in the images. Specifically, we extracted all the leaf pixels with PRI > -0.058 and all panicle pixels with PRI ≤ -0.058. Then, the pixels of sunlit leaves and shaded leaves were identified with TCARI values greater and less than 0.172, respectively; the sunlit and shaded panicles were identified with a TCARI value of greater and lower than 0.241, respectively. More detailed information regarding the discrimination of different components within rice canopies could be found in Zhou et al. (2017).

We calculated the green fraction from the original images with 1.3 mm spatial resolution for which the fraction of mixed pixels was negligible. Then, we followed the strategy in Jay et al. (2017) to adjust the threshold values of EVI, TCARI, PRI for individual resolutions to keep the green fraction close to that calculated at the 1.3 mm spatial resolution. As shown in **Fig. 4**, the EVI threshold values decreased as the spatial resolution degraded for the early tillering stage and the late tillering stage but slightly increased for the reproductive stages. In contrast, TCARI threshod values exhibited a tendency to decline from 2 mm resolution to 225 mm resolution for each stage. The PRI threshold values increased with the degradation of spatial resolution for the heading stage but decreased for the filling stage. Given only one pixel left when degrading the original cropped image to 450 mm spatial resolution, we did not provide the separate thresholds for this resolution. Additionally, the average spectra of all-leaf pixels, sunlit- and shaded-leaf pixels for 450 mm spatial resolution were assigned as the average spectra of whole-image pixels (vegetation pixels and background pixels) across the original cropped image (1.3 mm spatial resolution). Example classified images obtained from two contrasted stages for different spatial resolutions were illustrated in **Fig. 5**.

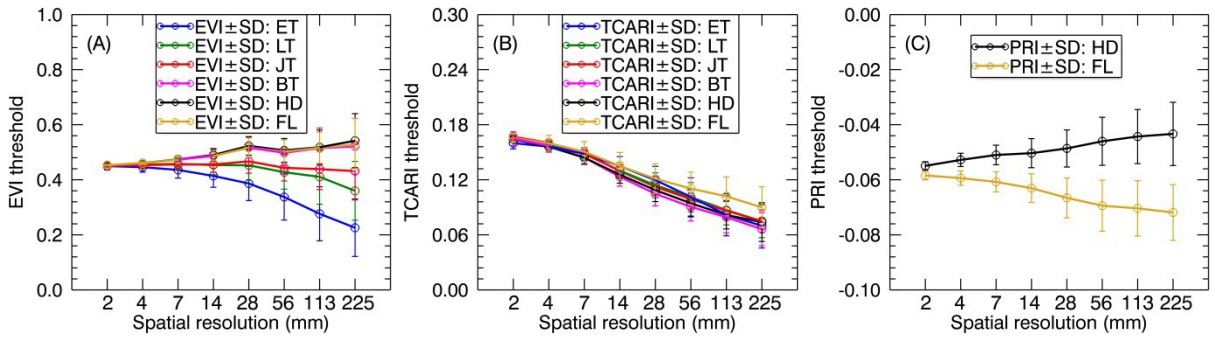

Fig. 4. The profiles of EVI (A), TCARI (B) and PRI (C) threshold values adjusted for coarser resolutions to keep the similar green fraction. ET: early tillering stage; LT: late tillering stage; JT: jointing stage; BT: booting stage; HD: heading stage; FL: filling stage.

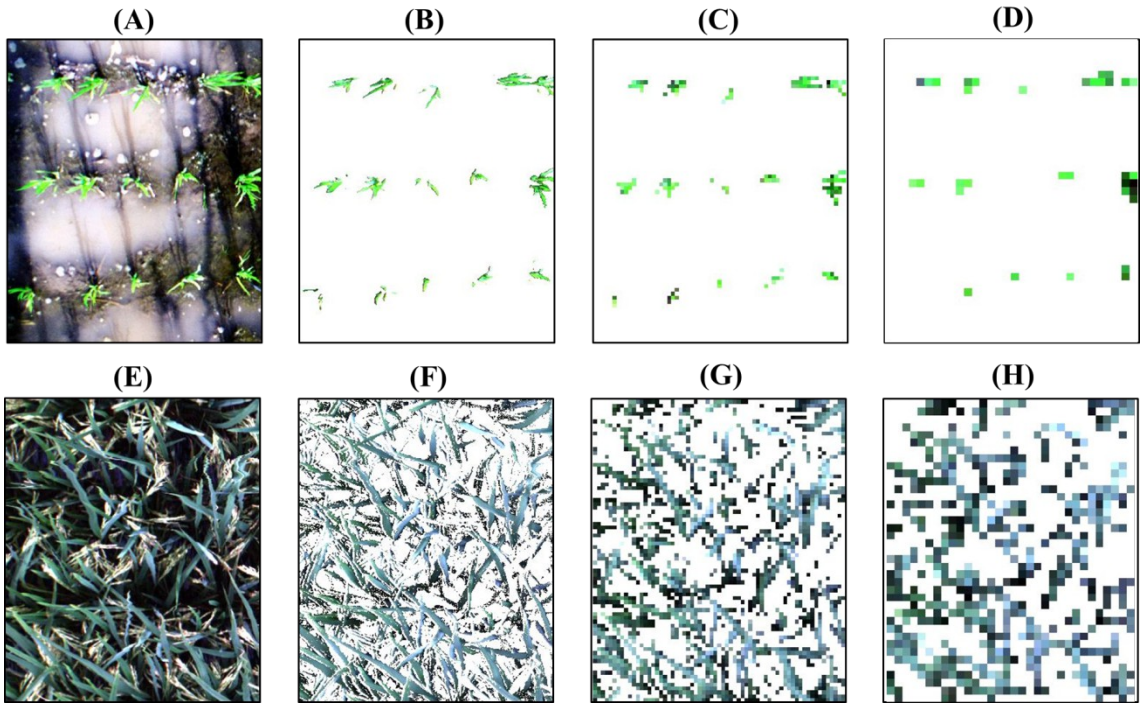

Fig. 5. Example classified images obtained from two contrasted stages, i.e., low green fraction for the early tillering stage (A), and large green fraction for the late filling stage (E). The resulting discrimination results are illustrated for 1.3 mm (B, F), 7 mm (C, G) and 14 mm (D, H) spatial resolutions. The white background represents non-vegetation pixels or panicle pixels.

2.4. Calculation of VIs

VIs are designed with band combinations to amplify their sensitivity towards particular biochemical or biophysical parameters and while also minimize the possible confounding effects (Malenovský et al. 2015). We included indices from the literature, specifically the evaluation of N status of crops based on leaf and canopy level reflectance. We selected three types of published VIs, including the ratio indices, the normalized difference indices and the combined vegetation indices to estimate LNC as listed in **Table 3**. The band selection for each index was deliberately implemented as suggested in Yu et al. (2013) by involving different spectral range for blue, red, green, red-edge and NIR.

Table 3

Published VIs related to N status of crops used in this study.

Index	Equation	Reference
Simple ratio indices		
SR[800, 675]	R_{800}/R_{675}	Jordan (1969)
SR[810, 560]	R_{810}/R_{560}	Xue et al. (2004)
SR[750, 550]	R_{750}/R_{550}	Kim et al. (1994)
SR[750, 710]	R_{750}/R_{710}	Zarco-Tejada et al. (2001)
$CI_{Red\text{-}edge}$	R_{800}/R_{720} -1	Gitelson et al. (2003)
Normalized difference indices		
NDVI	$(R_{800}-R_{670})/(R_{800}+R_{670})$	Rouse et al. (1974)
GNDVI	$(R_{750}-R_{550})/(R_{750}+R_{550})$	Gitelson et al. (1996)
ND705	$(R_{750}-R_{705})/(R_{750}+R_{705})$	Gitelson and Merzlyak (1994)
mND705	$(R_{750}-R_{705})/(R_{750}+R_{705}-2*R_{445})$	Sims and Gamon (2002)
mSR705	$(R_{750}-R_{445})/(R_{705}-R_{445})$	Sims and Gamon (2002)
MTCI	$(R_{750}-R_{710})/(R_{710}-R_{680})$	Dash and Curran (2004)
PRI	$(R_{531}-R_{570})/(R_{531}+R_{570})$	Gamon et al. (1992)
Combined difference indices		
TCARI	$3*[(R_{700}-R_{670})-0.2*(R_{700}-R_{550})(R_{700}/R_{670})]$	Haboudane et al. (2002)
OSAVI	$(1+0.16)(R_{800}-R_{670})/(R_{800}+R_{670}+0.16)$	Rondeaux et al. (1996)
TCARI/OSAVI	TCARI/OSAVI	Haboudane et al. (2002)
DCNI	$(R_{720}-R_{700})/(R_{700}-R_{670})/(R_{720}-R_{670}+0.03)$	Chen et al. (2010)

2.5. Multivariate methods

Using multivariable methods is helpful for taking advantage of hyperspectral data with large number of wavebands at fine spectral resolution (Inoue et al., 2012).

2.5.1. Partial least squares regression (PLSR)

PLSR (Martens and Næs, 1998; Wold et al., 2001) is one of the reliable analytical tools for multivariable data analysis and have been widely used in the assessment of crop nitrogen status (Vigneau et al., 2012; Inoue et al., 2012; Ecarnot et al., 2013; Yu et al., 2014). It possesses an advantage to avoid high multi-collinearity among variables, which is the inherent issue in multiple stepwise regression (Inoue et al., 2012). When compared with multiple stepwise regression or principal component, PLSR generally exhibits better predictive performance (Ye et al., 2008; Ecarnot et al., 2013; Yu et al., 2014). Specifically, PLSR models are built based on latent vari-

ables instead of real variables (Yu et al., 2014).

2.5.2. Gaussian Process regression (GPR)

GPR is a nonparametric method that learns the relationship between the input variables (e.g., reflectance) and output parameters (e.g., LNC) by fitting a flexible probabilistic (Bayesian) model directly in function space, with no intermediate model or model parameters (Verrelst et al., 2012; Verrelst et al., 2013). Over the last decade, GPR has emerged as an effective machine learning approach to retrieving biophysical parameters (Verrelst et al., 2012; Verrelst et al., 2013; Verrelst et al., 2016). In particular, GPR has been used for mapping leaf area index and fractional vegetation cover (Verrelst et al., 2012) and quantifying vegetation traits such as leaf chlorophyll content (Verrelst et al., 2012; Verrelst et al., 2013) and canopy water content (Verrelst et al., 2016).

GPR has alleviated some shortcomings of similar machine learning methods, while generally achieving good predictive performances and stabilities. For example, training GPR is far simpler than neural networks or support vector machines by using very flexible kernels with several free parameters. Furthermore, GPR provides a ranking of features (e.g., wavelengths) and samples (e.g., reflectance spectra) and thus partly overcoming the blackbox problems encountered in nonparametric regression methods (Verrelst et al., 2012).

2.5. LNC measurements

After each measurement of canopy hyperspectral images, three clusters of plants at the center of the spectral sampling area from each plot were selected randomly and destructively sampled for the determination of leaf weight and LNC. For each sample, all green leaves were separated from their stems, and oven-dried for 30 minutes at 105°C, and then for about 24 hours

189at 80°C till constant weight. Dried leaf samples were ground and then stored in plastic bags prior
190to chemical analysis. LNC (%) was determined with micro-Keldjahl analysis method (Tian et al.,
1912014).

192*2.6. Calibration and validation of predictive models*

193 The predictive models were divided into two types: stage-specific and stage-nonspecific
194(i.e., global models that are suitable for the full season). Specifically, the stage-specific models
195for individual growth stages before booting or stage-groups after booting were constructed using
196simple linear or nonlinear regression analysis between LNC and VIs derived from the average
197spectra of all the leaf pixels, sunlit or shaded leaf pixels for individual spatial resolution datasets.

198 The global models were constructed using two multivariable methods: PLSR (Martens
199and Næs, 1998; Wold et al., 2001) and GPR (Rasmussen and Williams, 2006) based on the sam-
200ples across all growth stages. Specifically, we calibrated models between LNC and reflectance
201spectra (400-900 nm) or continuum-removed reflectance spectra (550-750 nm) (Kokaly et al.,
2022003) using PLSR and GPR, respectively. Additionally, we selected the optimal number of latent
203variables for calibrating the PLSR model by leave-one-out cross-validation on the calibration set.

204 Two replications for each treatment were used for calibrating predictive models (i.e., 2/3
205of the samples used as the calibration samples) and one replication (i.e., 1/3 of the samples used
206as the validation samples) were used for validating the models. With regard to the stage-specific
207models, there were 24 calibration samples and 12 validation samples for individual growth stages
208before booting but 144 calibration samples and 72 validation samples for the stage-group after
209booting (i.e., reproductive stages). For the global models, there were 288 calibration samples and
210144 validation samples through the whole growing season. The performance of models was as-

sessed using the predictive coefficient of determination (R^2), root mean square error (RMSE) between the measured and predicted LNC values.

2. Results

3.1 Seasonal variation in LNC and spectral properties of all-leaf pixels and whole-image pixels

Fig. 6 shows the statistics of LNC measurements for individual growth stages in 2014 and 2015. Generally, the LNC values for 2014 and 2015 decreased from 4.29 % to 1.36 % with the development of growth stages. For both years, LNC changed dramatically from early tillering to jointing stages.

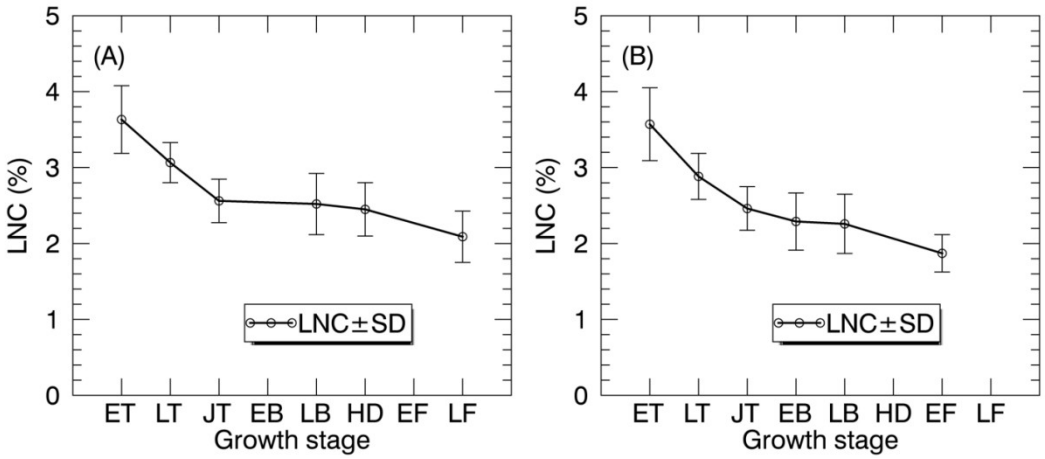

Fig. 6. The temporal profiles of LNC in paddy rice over the whole season in 2014 (A) and 2015 (B). ET: early tillering stage; LT: late tillering stage; JT: jointing stage; EB: early booting stage; LB: late booting stage; HD: heading stage; EF: Early filling stage; LF: Late filling stage.

Regardless of spectral datasets for all-leaf pixels and whole-image pixels, the average reflectance of all plots in the visible region decreased from the early tillering stage to the booting or heading stage and then raised until the filling stage (**Fig. 7**). However, the reflectance in the NIR region showed an opposite tendency as compared to the visible region. With regard to the

comparison between the reflectance spectra of all-leaf pixels and whole-image pixels for individual stages, the NIR reflectance spectra averaged over all the leaf pixels exhibited higher amplitudes than those averaged over all canopies, especially during the early growth stages.

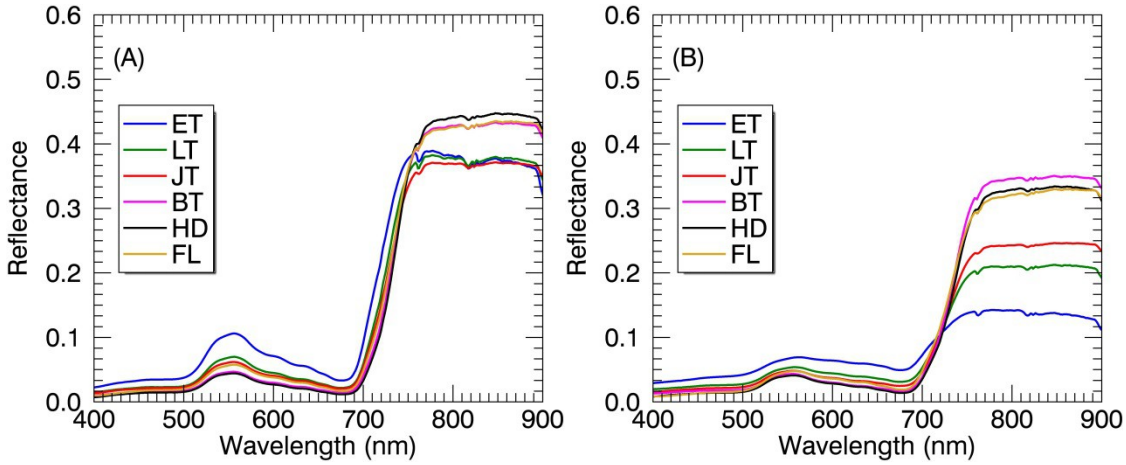

Fig. 7. Mean reflectance spectra derived from all leaf pixels (A) and all image pixels (B) at individual growth stages. Plots represent the combined data from 2014 and 2015. ET: early tillering stage; LT: late tillering stage; JT: jointing stage; BT: booting stage (including early and later booting stages); HD: heading stage; FL: filling stage (including early and later filling stages).

3.2 Relationships of rice LNC with VIs derived from all-leaf pixels and whole-image pixels for various stages

Table 4 shows a summary of squared Spearman's correlation coefficients for all VIs relating to LNC by growth stage. From the early tillering stage to the jointing stage, most of the correlations (p<0.05) for the VIs derived from all-leaf pixels exhibited higher R^2 values than those derived from whole-image pixels. This contrast generally became less significant with the development of growth stages but was still apparent at the group of reproductive stages. Among

Table 4

Squared correlation coefficients (ρ^2) from Spearman's correlation for the relationships between LNC and VIs derived from all-leaf pixels or whole-image pixels (leaf + background pixels) of the original images at 1.3 mm spatial resolution for individual growth stages in the vegetative period and the group of reproductive stages.

VIs	Early tillering		Late tillering		Jointing		Reproductive	
	Leaf pixels	Leaf +background pixels	Leaf pixels	Leaf +background pixels	Leaf pixels	Leaf +background pixels	Leaf pixels	Leaf +background pixels
Simple ratio								
SR[800, 675]	0.27**	0.27**	0.43**	0.23**	0.42**	0.37**	0.43**	0.28**
SR[810, 560]	0.49**	0.29**	0.46**	0.28**	0.58**	0.47**	0.64**	0.46**
SR[750, 550]	0.49**	0.26**	0.45**	0.27**	0.55**	0.44**	0.59**	0.40**
SR[750, 710]	0.69**	0.35**	0.59**	0.34**	0.66**	0.52**	0.67**	0.53**
$CI_{Red\text{-}edge}$	**0.71****	0.39**	0.61**	0.40**	0.67**	0.58**	0.70**	0.61**
Normalized difference index								
NDVI	0.27**	0.27**	0.41**	0.23**	0.42**	0.37**	0.47**	0.31**
GNDVI	0.49**	0.26**	0.45**	0.27**	0.55**	0.44**	0.59**	0.40**
ND_{705}	0.69**	0.35**	0.60**	0.31**	0.64**	0.49**	0.65**	0.50**
mND_{705}	0.62**	0.39**	0.69**	0.36**	0.69**	0.57**	**0.71****	0.59**
mSR_{705}	0.62**	0.39**	0.69**	0.36**	0.69**	0.57**	**0.71****	0.59**
MTCI	0.70**	0.41**	0.64**	0.52**	0.69**	**0.63****	**0.71****	**0.63****
PRI	0.05	0.12*	0.01	0.08	0.08	0.29**	0.51**	0.36**
Combined difference index								
TCARI	0.42**	0.06	0.64**	0.01	**0.75****	0.06	0.66**	0.33**
OSAVI	0.15**	0.25**	0.07	0.18**	0.37**	0.39**	0.36**	0.22**
TCARI/OSAVI	0.64**	**0.47****	**0.76****	**0.67****	0.72**	0.60**	0.69**	0.52**
DCNI	0.48**	0.28**	0.62**	0.49**	**0.75****	0.56**	0.63**	0.48**

* $P<0.01$; ** $P<0.001$. The highest correlations in each column are highlighted in bold.

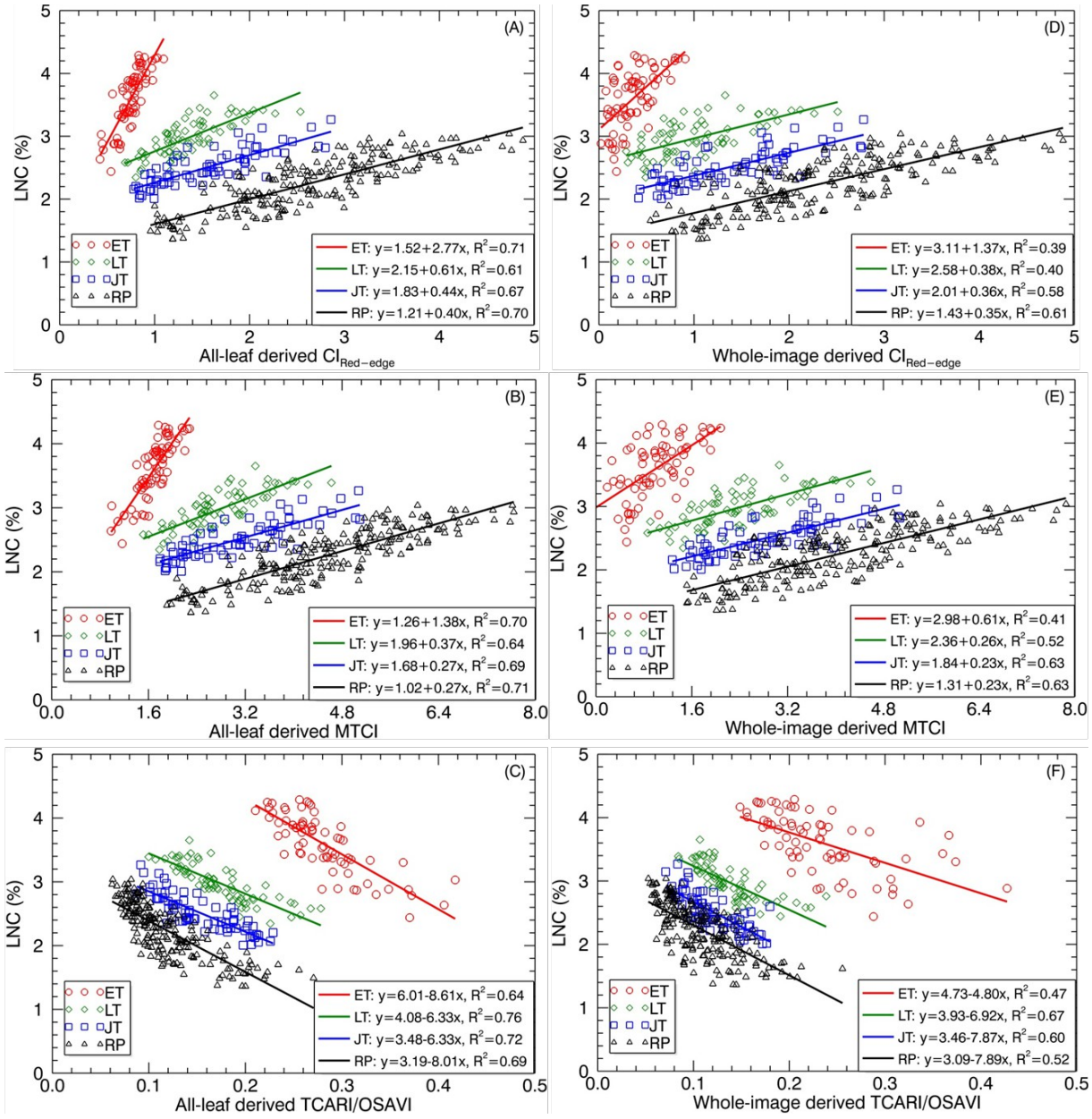

Fig. 8. Best-fit linear relationships of LNC with three representative VIs derived from all-leaf pixels and whole-image pixels: (A; D) $CI_{Red-edge}$, (B; E) MTCI and (C; F) TCARI/OSAVI across the original cropped images at 1.3 mm spatial resolution. ET: early tillering stage; LT: late tillering stage; JT: jointing stage; RP: reproductive stages (stages after booting).

the VIs examined, the ones employing red-edge bands (i.e., SR[750, 710], ND_{705}, mSR_{705}, MTCI,

253mND$_{705}$, CI$_{Red\text{-}edge}$) displayed higher R^2 values than others. CI$_{Red\text{-}edge}$, MTCI and TCARI/OSAVI
254represented the best performing VIs for the three groups, respectively. With regard to the perfor-
255mance of these three representative VIs, TCARI/OSAVI generally exhibited higher ρ^2 than CI$_{Red\text{-}}$
256$_{edge}$ and MTCI at the late tillering stage but lower ρ^2 at the reproductive stages. In contrast, these
257three VIs exhibited similar ρ^2 values for remaining two stages (early tillering and jointing).

258 **Fig. 8** shows the scatter plots of LNC~VI models with three representative VIs derived
259from all-leaf pixels and whole-image pixels for different growth stages. Within both all-leaf pix-
260els and whole-image pixels represented by the three VIs, the LNC~VI models were different
261among the first three stages and another single model could fit for the remainder (reproductive
262phase) of growth stages. From early tillering to reproductive stages, the LNC decreased substan-
263tially but the VIs did not follow the decrease, which led to the presence of four clusters in each of
264the scatter plots. Specifically, the scatter plots of the VIs derived from all-leaf pixels were more
265concentrated than those of the VIs derived from whole-image pixels for any of the stages before
266booting, with the most significant discrepancy being for the early tillering stage. While the
267LNC~VI models for the stages of late tillering and jointing exhibited similar slopes to those for
268the reproductive stages, the models for the early tillering stage differed from all of them in slope
269and intercept. These model differences between stages precluded the data from being fitted with
270a global model for the whole season. A multi-stage model was possible only for data from the
271post-booting stages as shown in **Fig. 8** and **Table 4**. For the correlations with LNC in the pooled
272data over reproductive stages, most indices derived from all-leaf pixels exhibited marginal differ-
273ences in R^2 as compared to those derived from whole-image pixels except TCARI.

274*3.3 Sensitivity of the stage-specific LNC~VI relationships to spatial resolution*

275 **Fig. 9** shows the sensitivity (in terms of ρ^2) of LNC~VI relationships (derived from leaf

pixels, sunlit and shaded leaf pixels) to spatial resolution for different growth stages. Generally, the correlations of VIs with LNC decreased with the degradation of spatial resolutions at a specific stage (or stage-group). Specifically, most ρ^2 values for the early tillering stage remained nearly stable from 1.33 mm to 14 mm spatial resolutions, except for a maximum (ρ^2 = 0.73 as the

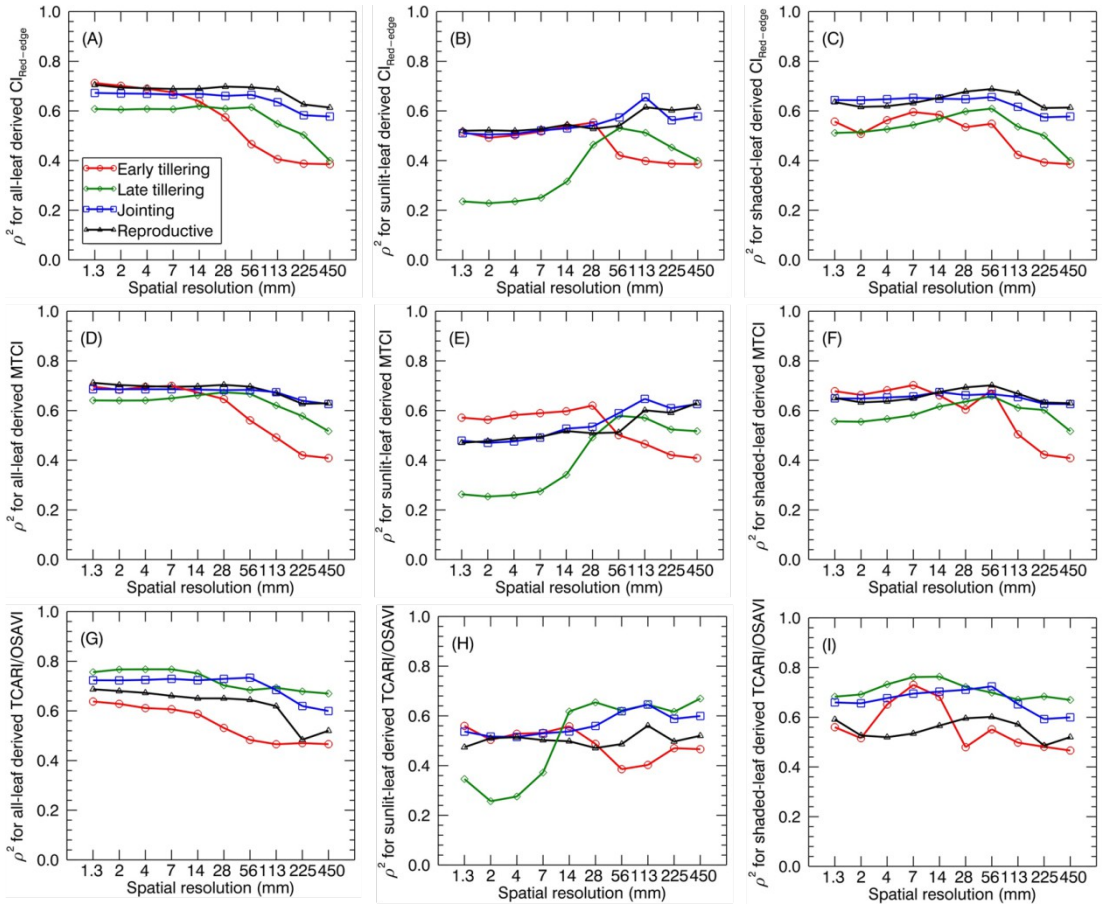

Fig. 9. The squared Spearman's correlation (ρ^2) between three representative VIs as a function of spatial resolution. VIs are derived from the average reflectance spectra of all-leaf pixels, sunlit- and shaded- leaf pixels across the whole image for different growth stages. The VIs for all-leaf pixels, sunlit- and shaded-leaf pixels at 450 mm spatial resolution were all calculated from the average reflectance spectra of whole-image pixels.

highest value for the early tillering stage) being observed at 7 mm spatial resolution for

TCARI/OSAVI derived from shaded leaf pixels. In contrast, most ρ^2 values decreased substantially from 14 mm to 450mm spatial resolution regardless of leaf pixel types. The changing patterns of ρ^2 for the late tillering, jointing and reproductive stages were generally similar to that of the early tillering stage except the decline starting from 56mm spatial resolution for VIs derived from leaf pixels and shaded leaf pixels but from 113mm spatial resolution for VIs derived from sunlit leaf pixels.

Comparing three types of leaf pixels, most VIs of sunlit leaves displayed weaker relationships with LNC than those of all leaves and shaded leaves. In particular, VIs of sunlit leaves exhibited much lower correlations with LNC at the late tillering stage for 1.3 mm ~ 14 mm spatial resolution (ρ^2 = 0.23~0.62). In contrast, more stable values of ρ^2 were observed for considering all-leaf pixels over different spatial resolutions. Especially, MTCI derived from all-leaf pixels exhibited closet ρ^2 between different spatial resolutions at specific stages.

As shown in **Table 5**, the best performing VI for all the individual stages before booting was TCARI/OSAVI. In particular, the best models were observed at a finer resolution for the early tillering stage (shade leaf pixels at 7 mm spatial resolution) and the late tillering stage (leaf pixels at 4 mm spatial resolution) but at a coarser resolution for the jointing stage (leaf pixels at 56 mm spatial resolution). For the reproductive stages, MTCI derived from leaf pixels at 28 mm spatial resolution performed better than other situations.

Table 5

The prediction accuracies for the best-fit linear relationships between LNC and a specific VI from three representative VIs at a specific spatial resolution for the early tillering stage, the late tillering stage, the jointing stage and the reproductive stages.

Growth stages	Best VIs	R^2	RMSE (%)
Early tillering	TCARI/OSAVI (Shaded-leaf pixels, 7 mm)	0.65	0.25
Late tillering	TCARI/OSAVI (All-leaf pixels, 4 mm)	0.66	0.18
Jointing	TCARI/OSAVI (All-leaf pixels, 56 mm)	0.67	0.18
Reproductive stages	MTCI (All-leaf pixels, 28 mm)	0.72	0.23

3.4 Sensitivity of global LNC predictions to spatial resolution

When applying the global models (i.e., stage-nonspecific models for all stages) to the validation dataset, the prediction accuracies generally decreased with the degradation of spatial resolution. The R^2 for all-leaf pixels slightly changed from 1.3 mm to 28 mm (e.g., R^2 = 0.69~0.72 for GPR using reflectance spectra of leaf pixels) and then gradually decreased. Specifically, leaf pixels exhibited more stable predictive accuracies over different spatial resolutions (R^2 = 0.55~0.73 for GPR; R^2 = 0.50~0.63 for PLSR) than sunlit leaf pixels (R^2 = 0.43~0.75 for GPR; R^2 = 0.45~0.63 for PLSR) and shaded leaf pixels (R^2 = 0.53~0.68 for GPR; R^2 = 0.42~0.60 for PLSR). In contrast, the accuracies for the sunlit leaf pixels dramatically declined with the degradation of spatial resolutions after 7 mm spatial resolution. In particular, sunlit leaf pixels produced the best prediction of LNC at 1.3 mm ~ 4 mm spatial resolution (R^2 > 0.74, RMSE < 0.33 %) while performing GPR regardless of using reflectance spectra and continuum-removed reflectance spectra.

GPR generally exhibited higher R^2 and lower RMSE values than PLSR regardless of

spectral information derived from all-leaf pixels, sunlit-leaf pixels and shaded-leaf pixels (**Fig. 11**). With regard to reflectance spectra and continuum-removed spectra, the former generally showed better predictive performances than the latter for PLSR but similar accuracies for GPR. Specifically, the reflectance spectra of shaded-leaf pixels exhibited higher R^2 as compared to the continuum-removed spectra of shaded-leaf pixels when performing GPR.

Fig. 12 shows the band-by-band values of parameter σ for GPR models and regression coefficients for PLSR models from degraded imaging data with 28 mm spatial resolution, which is optimal for generating stable predictive performance. In the case of GPR model, the band with the lowest σ represents the most contribution to the regression model. As shown in **Fig. 12**, most contributing bands were located around the red region (680 nm), red-edge region (700 nm), the blue region (420 nm), the green region (520 nm, 560 nm) regardless of leaf pixel types. Specifically, leaf pixels generally exhibited lower σ values than sunlit and shaded leaf pixels over all the wavelengths. In contrast, the highest σ values were observed in the near-infrared shoulder region for sunlit leaves.

For PLSR models, the importance of each band was evaluated by the coefficient values. The important bands (coefficients in absolute value) for PLSR models were found around the similar region as compared with the GPR models. The absolute coefficient values for all-leaf pixels were generally higher than sunlit- and shaded-leaf pixels. However, there were not substantial differences in the coefficients of PLSR models among three types of leaf pixels in the near-infrared shoulder region.

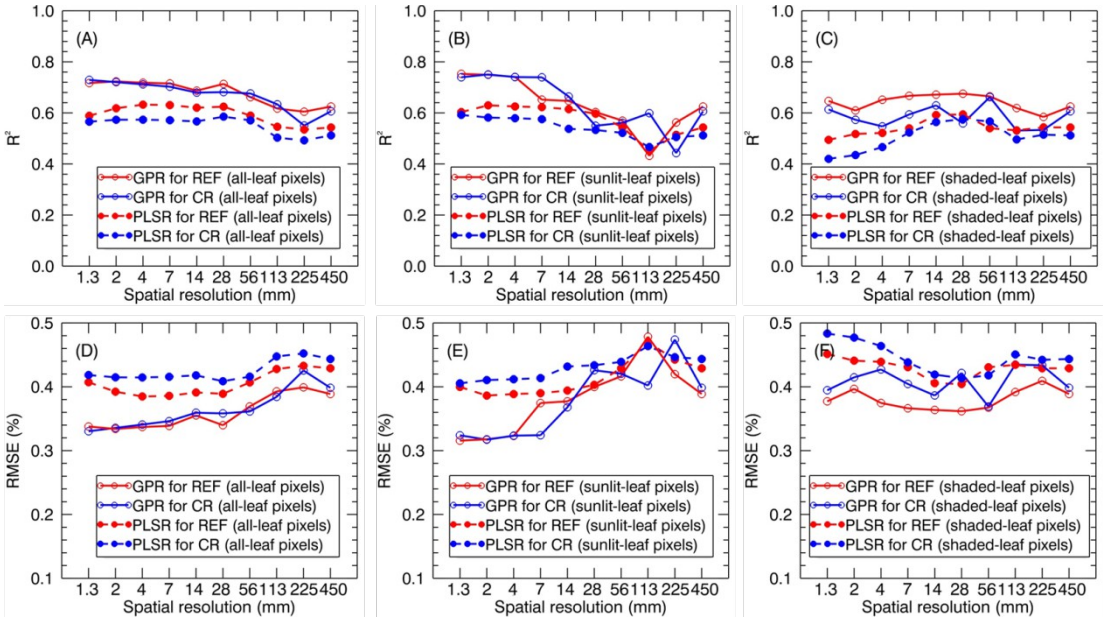

Fig. 11. LNC prediction accuracies for GPR and PLSR using reflectance spectra (REF) and continuum-removed spectra (CR) derived from all-leaf pixels (A; D), sunlit-leaf pixels (B; E) and shaded-leaf pixels (C; F).

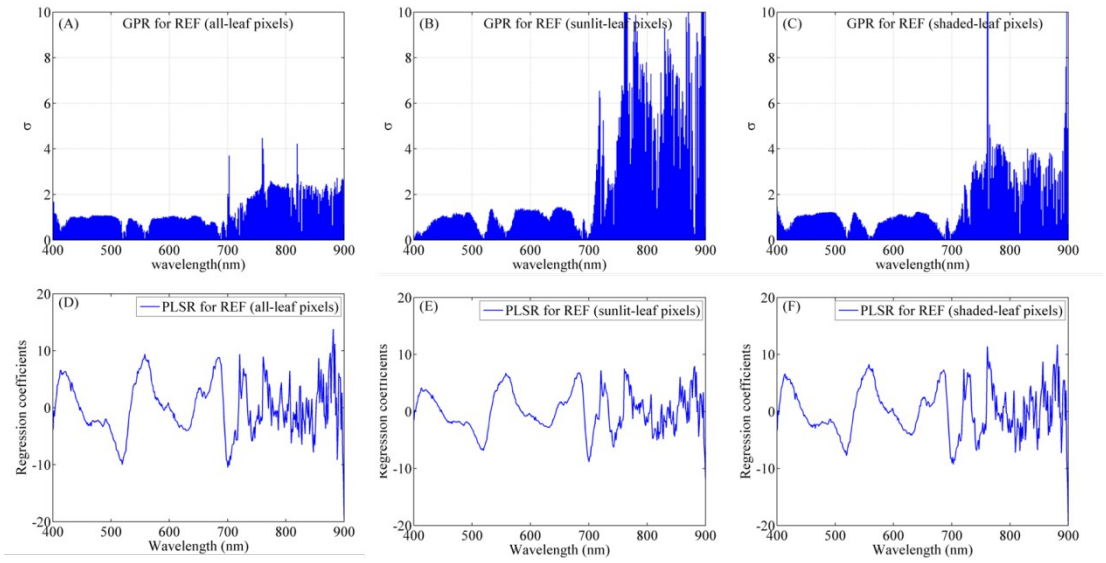

Fig. 12. The dedicated parameter σ of each band for GPR and the regression coefficient of each band for PLSR using average spectra of all-leaf pixels (A; D), sunlit-leaf pixels (B; E) and shaded-leaf pixels (C; F) from imaging data with 28 mm spatial resolution.